Photonic crystal fiber-based plasmonic sensors for the detection of biolayer thickness

Alireza Hassani and Maksim Skorobogatiy*

Department of Engineering Physics, École Polytechnique de Montréal, C.P. 6079, Succursale Centre-Ville, Montréal H3C 3A7, Canada
**Corresponding author: maksim.skorobogatiy@polymtl.ca*

Received January 21, 2009; revised May 21, 2009; accepted May 26, 2009;
posted May 29, 2009 (Doc. ID 106603); published July 8, 2009

The application of metallized photonic crystal fibers in surface plasmon resonance sensors of biolayer thickness is demonstrated. By the judicious design of photonic crystal fibers, the effective refractive index of the fundamental core mode can be tuned to enable efficient phase matching with a plasmon anywhere from the visible to near IR. Among other advantages of the presented sensors we find high sensitivity in the visible and near-IR spectral regions, as well as high coupling efficiency from an external Gaussian beam. Based on the numerical simulations, we present designs using various types of photonic crystal fibers, including holey fibers with and without defect, as well as honeycomb photonic crystal fibers. We find that in addition to the fundamental plasmonic excitation, higher order plasmonic modes can also be excited. In principle, using several plasmonic excitations at the same time can enhance sensor detection limit. Both amplitude and spectral-based methodologies for the detection of changes in the biolayer thickness are discussed. Sensor resolutions of the biolayer thickness as high as 0.039–0.044 nm are demonstrated in the whole 600–920 nm region. Finally, we perform analysis of the effect of imperfections in the metal layer geometry on the sensor sensitivity. © 2009 Optical Society of America

OCIS codes: 130.6010, 240.6680, 050.5298.

1. INTRODUCTION

Surface plasmon resonance (SPR) is a prominent optical phenomenon, which involves resonant excitation of electromagnetic surface waves coupled with collective oscillations of free electrons in metal. When excited over a metal/liquid interface, the plasmons offer attractive applications in biosensing. In a bulk sensor geometry, SPR is produced with the help of a prism in the Kretschmann–Raether arrangement [1], where *p*-polarized light is launched into a glass prism and then reflected from a gold-covered prism facet in contact with a liquid analyte. The point of phase matching (specific combination of the angle of incidence and wavelength) between the probing photon and a plasmon is detected through the observation of a dip in the reflectivity. Since phase matching condition depends resonantly on the refractive index of analyte within ~100 nm from the gold surface [2] (when operated in the visible spectral range), the method enables detection of extremely small variations in the refractive index in the vicinity of a metal surface by following angular [3,4], spectral [5], or phase [6,7] characteristics of the reflected light. By activating the metal surface with biomolecules that can selectively bind the target molecules and by observing the changes in the thickness and refractive index of thus formed biolayer, one can detect minute concentration of the analyte molecules. Due to the resonant nature of SPR transduction and the absence of labeling step, this method has quickly become a technology of choice for the label-free detection of various biomolecules and chemical molecules [8]. However, the high cost and large size of most commercially available systems make them useful only in a laboratory setting, while many important applications requiring portability remain out of reach for this method.

To miniaturize SPR biosensors and to reduce their cost, several waveguide-based systems have been proposed [9–15]. In such integrated SPR sensors, one launches light into a waveguide core and then uses coupling of the fundamental core mode with a plasmon propagating over a thin metal film deposited onto some part of the same waveguide. An effective refractive index of a waveguide core mode is typically similar to that of a core material, which for most materials is larger than 1.45. At frequencies significantly lower than the metal plasma frequency (for gold, the plasmon frequency is in the ~500 nm range), the effective refractive index of a plasmon is close to that of a bordering aqueous analyte (1.33). Only at frequencies approaching the metal plasma frequency can the plasmon refractive index become significantly larger than that of a bordering analyte. Mathematically, the phase matching condition between the core-guided and plasmon modes implies matching the modal refractive indices. From the discussion above it follows that such a phase matching is difficult to achieve for aqueous analytes when operating at frequencies much lower than the metal plasma frequency. Thus, due to practical limitations on the waveguide core material refractive index, integrated SPR sensors for aqueous analytes typically operate in the

 © 2009 Optical Society of America

immediate vicinity of the plasma frequency of a metal layer. This, in turn, limits the probe depth of the integrated sensors to ~100 nm from the metal surface.

For the sensor to be effective the size of a biolayer has to be smaller or comparable to the sensor probing depth, otherwise changes in the biolayer structure cannot be detected. Probing depths ~100 nm are well suited for the detection of binding dynamics of most proteins having diameters in the range 4–10 nm. Protein detection typically involves activation of the sensor metal surface with the antibodies (proteins of 4–10 nm in diameter) that are specific to capturing only the target proteins via a so-called "lock-key" mechanism. In the case of protein detection sensing is effective as the total biolayer size does not exceed ~20–30 nm. When operating in the visible spectral range, the detection of larger biomolecules, such as viruses (size range 10–100 nm) and bacteria (size range of $1-100\mu$m), becomes problematic owing to the particle large sizes. For example, to detect bacteria one can activate the sensor metal surface with viruses (phages), which are specific to binding a particular bacteria. As a typical virus size is in the 50 nm range, the overall biolayer thickness becomes comparable or larger than the probing depth of a plasmon, thus reducing the sensor sensitivity. To extend the application of SPR sensing to the detection of larger biomolecules, one should increase the plasmon probing depth, which implies operation at longer wavelengths.

To enable SPR sensors for the detection of larger biomolecules, we have recently proposed theoretically the use of photonic crystal waveguides [16,17] and fibers [18–22] containing metallic layers in their cross section and operating in the near IR. Experimental progress in the fabrication of such structures was recently reported in [23–26]. Plasmon excitation in microstructured fibers with gold and silver nanowires have been recently demonstrated in [27,28]. In such metallized photonic crystal waveguides, the effective refractive index of the fundamental core mode can be reduced at will, which allows phase matching the core-guided and plasmon modes at practically any desired wavelength of operation. In our prior works we have concentrated on the characterization of the sensitivity of integrated SPR sensors to the changes in the analyte bulk refractive index. In this work we investigate the sensitivity of several such sensors with respect to the changes in the thickness of a biolayer deposed onto a waveguide surface, which is more relevant to the biomolecule detection applications. Moreover, in this work we demonstrate the possibility of tuning a plasmonic mode via introduction of defects into the waveguide cladding in the vicinity of a metal layer. Furthermore, the effect of inhomogeneities in the structure of a metal layer on the sensitivity of a sensor is studied. Finally, we demonstrate the possibility of excitation of higher order plasmon modes on a circular surface of a metallized fiber, and we discuss the potential of using such modes to enhance sensor sensitivity.

This paper is organized as follows. In the first part we study the sensitivity of the SPR sensors based on the total internal reflection (TIR) holey fibers. We then investigate how structural defects in the fiber geometry can be used to tune a plasmon mode. Finally, we conclude the first part by studying the effect of the metal film nonuniformity on the sensor sensitivity. In the second part, we characterize the sensitivity of a honeycomb photonic bandgap fiber-based SPR sensor. We then demonstrate the possibility of having several plasmon excitations, which span the frequencies from the visible to near IR in the same sensor.

2. MICROSTRUCTURED FIBER-BASED SURFACE PLASMON RESONANCE BIOSENSORS

In this section we investigate the sensitivity of the microstructured optical fiber (MOF)-based sensors of a biolayer thickness. The underlying fibers used in such sensors guide using TIR. Figures 1(a) and 1(b) show the two schematics of the proposed hexagonal solid-core MOF-based SPR sensors. Both designs feature two large semicircular channels containing analyte. Thin gold films are deposited on one side of the channels closer to the fiber core. In the second MOF design, three small holes are added in the fiber cross section. The holes are placed in the near vicinity of the gold layer to study tuning a plasmon mode by varying the hole geometry.

To lower the effective refractive index of the core-guided mode (in order to facilitate phase matching with a

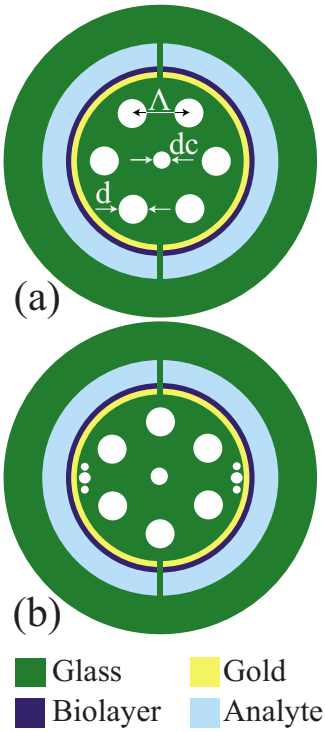

Fig. 1. (Color online) Schematics of the two MOF-based SPR biosensors (a) without and (b) with the air hole defects in the near vicinity of the gold layers. In both cases, one layer of the air filled holes is used to confine light in the fiber core and to control the coupling strength between the core mode and a plasmon wave. Small air filled hole in the fiber core is used to lower the refractive index of a core-guided mode to facilitate phase matching with a plasmon. Two large semicircular metallized channels are integrated into the fiber structure to enable the flow of analyte. In design (b), structural defects in the form of three small holes are placed near the gold film and are used to tune a plasmon mode.

plasmon), we introduce a small hole of diameter d_c into the fiber core center. All the holes in the fiber cross section are filled with air $n_{air}=1.0$, while metal covered semicircular channels are filled with analyte (aqueous solution) $n_a \simeq 1.33$. In both designs we consider the diameters of the six holes surrounding the fiber core to be $d=0.6\Lambda$, while the diameter of a central hole is taken to be $d_c=0.45\Lambda$. The pitch of an underlying hexagonal lattice is $\Lambda=2$ μm. Three defect holes in the design of Fig. 1(b) have diameters $d/8$, $d/4$, and $d/8$, with the central hole being the largest; the center of the large central hole is located $(d\cdot 3/16)$ from the gold surface. By changing the size of a central hole, one can tune the effective refractive index of the fundamental core mode. The semicircular channels of the fibers are metallized with a thin gold layer and feature large sizes to facilitate the flow of analyte. The channel size (difference in the inner and outer radii) is 1.5Λ, while the thickness of the bridge connecting the fiber core and cladding regions is $d_c/4$. Finally, we assume that MOF is made of a silica glass with refractive index given by the Sellmeier equation. The dielectric constant of gold ϵ_{Au} is approximated in the visible and near-IR region by the Drude model [29] $\epsilon_{Au}(\omega)=\epsilon^{\infty}-\omega_p^2/[\omega(\omega+i\omega_\tau)]$, where $\epsilon^{\infty}=9.75$, $\omega_p=1.36\times 10^{16}$ rad/s and $\omega_\tau=1.45\times 10^{14}$ rad/s. The gold layer thickness is defined as d_{gold} and in this work is in the range 40–65 nm.

A. Case (a): Microstructured Optical Fiber-Based Sensor Without Defects

Finite element method with the perfectly matched layer (PML) boundaries was used to find complex propagation constants of the core-guided and plasmonic modes. A typical fiber-based plasmonic sensor operates in the vicinity of a phase matching point between the core-guided mode and a plasmon wave localized at the metallized surface.

For the first MOF-based sensor with $d_{gold}=50$ nm, $d_{bio}=0$ [Fig. 1(a)], the phase matching point is located at 660 nm where the difference between the real parts of the modal refractive indices of the core mode and a plasmon wave is the smallest. In the vicinity of a phase matching point the two modes become strongly mixed, with losses of a core-guided mode increasing dramatically due tranto the energy transfer into the lossy plasmon mode (see Fig. 2). In biosensing applications, one defines the sensitivity of the SPR sensor with respect to the ability to detect changes in the thickness d_{bio} of a thin biolayer of index n_{bio} deposited on top of the metal film; n_{bio} is generally between 1.4 and 1.42 for most biomolecules. As explained in the Introduction, such a layer might, for example, consist of the antibodies placed on a sensor surface to provide detection specificity. Core mode losses α[dB/cm] are presented in Fig. 2 for the two thicknesses of a biolayer $d_{bio}=0$ and $d_{bio}=10$ nm. Thus, by changing the biolayer thickness by only 10 nm the plasmon resonance peak shifts by $\sim$23 nm, which can be easily detected. Such a transduction mechanism can, thus, be used for the monitoring of formation of the nanometer-thin biolayers on top of a metallized sensor surface.

We now discuss two main approaches to the detection of changes in the biolayer thickness. The first method is a spectral-based method. Within this method, changes in the biolayer thickness are detected by measuring the displacement of a plasmonic peak in the absorption spectrum of a sensor. The sensitivity of spectral method is defined as

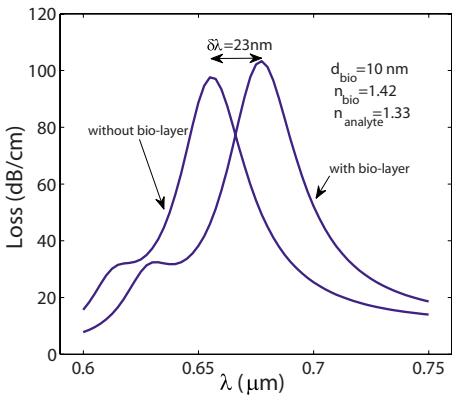

Fig. 2. (Color online) Loss spectra of the fundamental core-guided mode for the design shown in Fig. 1(a). Loss peaks correspond to the excitation of a plasmon mode on the surface of metallized channels filled with aqueous analyte $n_a=1.33$. Modal losses are shown for the biolayer thicknesses $d_{bio}=0$ and $d_{bio}=10$, assuming the biolayer refractive index $n_{bio}=1.42$. By changing the biolayer thickness one shifts the attenuation peak corresponding to the point of phase matching between the core-guided and plasmon modes.

$$S_\lambda[\text{nm nm}^{-1}]=\lim_{d_{bio}\to 0} d\lambda_{peak}/d_{bio}, \quad (1)$$

where $d\lambda_{peak}$ is a shift in the wavelength of the absorption peak center measured before and after the biolayer thickness is changed by d_{bio}. As an example, consider the sensor absorption spectra shown in Fig. 1, $d_{gold}=50$ nm. Using definition (1), we find the spectral sensitivity to be 2.3 nm nm^{-1}. It is typically a standard assumption that the 0.1 nm change in the position of a resonance peak $(d\lambda_{peak})$ can be detected reliably, which leads to the sensor resolution of 0.044 nm in biolayer thickness.

We now consider the second detection approach, which is known as the amplitude-based detection method. Within this method all the measurements are performed at a single wavelength. The advantage of this method is its simplicity and low cost compared with spectral-based methods, as no spectral acquisition is required. We now define the sensitivity of the amplitude-based detection method. Let $\alpha(\lambda,d_{bio})$ be the transmission loss of the fundamental core mode as a function of the wavelength of operation and biolayer thickness. Considering P_0 as the power launched into the fiber core mode, the power detected at the end of a sensor of length L will then be $P(L,\lambda,d_{bio})=P_0\exp(-\alpha(\lambda,d_{bio})L)$. At the operation wavelength λ, the amplitude sensitivity to the changes in the biolayer thickness can then be defined as $S_A(\lambda)[\text{nm}^{-1}]=\lim_{d_{bio}\to 0}|P(L,\lambda,d_{bio})-P(L,\lambda,0)|/P(L,\lambda,0)/d_{bio}$. The sensor length L is limited by the modal transmission loss. A reasonable choice of a sensor length is $L=1/\alpha(\lambda,d_{bio})$, which falls into a subcentimeter range for the MOFs described in this paper. The corresponding sensor volume is then sub-nL. This choice of a sensor length results in a simple definition of sensitivity for small changes in the biolayer thickness,

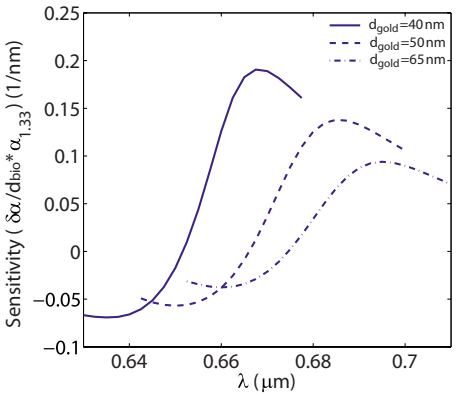

Fig. 3. (Color online) Sensitivity of the MOF-based sensors to changes in the biolayer thickness. Data are presented for sensors with the three different values of the gold layer thicknesses $d_{\text{gold}}=40$, 50, and 65 nm.

$$S_A(\lambda)[\text{nm}^{-1}] = -(\partial\alpha(\lambda,d_{\text{bio}})/\partial d_{\text{bio}})\alpha(\lambda,d_{\text{bio}}). \quad (2)$$

In Fig. 3 we present amplitude sensitivities of the proposed MOF-SPR sensors for the three different values of the gold layer thickness $d_{\text{gold}}=40$, 50, and 65 nm. Consider, for example, the case of a 40 nm thick film for which the maximum sensitivity to the changes in the biolayer thickness is equal to $\sim 0.2\ \text{nm}^{-1}$ and is achieved in the vicinity of 670 nm. By adding only a 1 nm thick biolayer the transmitted intensity of a sensor would change by $\sim 20\%$, which can be easily detected. It is typically a safe assumption that the 1% change in the transmitted intensity can be detected reliably, which leads to the sensor resolutions of 0.05 nm. We also observe that for thicker gold films sensor sensitivity decreases. This is simple to understand by noting that when the metallic layer thickness becomes larger than that of a metal skin depth ($\sim 20-30$ nm) fiber core mode becomes effectively screened from a plasmon mode, thus resulting in a low coupling efficiency and, as a consequence, in low sensitivity.

We now investigate the effect of nonuniformity in the thickness of a gold film on the sensitivity of a MOF-based sensor. Such nonuniformity is unavoidable in the realistic fabrication process, where metal film is produced either by deposition from a solvent phase or through chemical vapor deposition. As a model of nonuniformity we consider that the gold film is the thinnest near the material bridges suspending the fiber core region, while the film is the thickest toward the center of a microfluidic channel. As an example, we suppose that near the bridges the film thickness is 20 nm, while increasing linearly to 65 nm in the middle of the semicylindrical channels. The average layer thickness is therefore ~ 43 nm with over 20 nm variation around this value across the surface of a microfluidic channel. In Fig. 4, solid curves, we present the losses of the plasmonic modes of a MOF-based sensor featuring a nonuniform gold layer. The two plasmonic modes are for the two values of a biolayer thickness $d_{\text{bio}}=0$ and $d_{\text{bio}}=10$ nm. For comparison we present plasmonic peaks found in a system featuring a uniform 50 nm thick gold layer. As seen from the figure, the main effect of nonuniformity in the gold layer thickness is the flattening of a plasmonic peak, as well as the decrease in the maximum value of modal loss. Figure 5 shows the sensitivity of a sensor with a nonuniform metallic layer, as well as the sensitivities of the sensors with uniform layers of thicknesses 50 and 65 nm. Remarkably, even despite the 45 nm variation in the metallic layer thickness, the sensitivity of a sensor featuring a nonuniform metal layer is comparable to that of a sensor with a uniform layer of some average thickness. In Fig. 5 we also estimate a 0.087 nm resolution of a sensor with a highly nonuniform metallic layer.

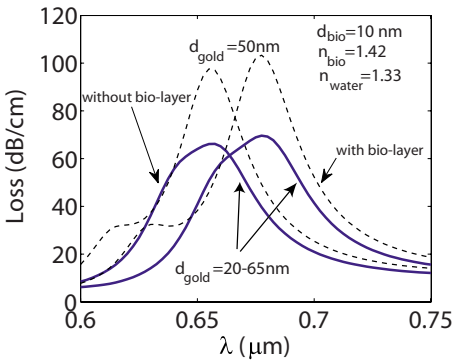

Fig. 4. (Color online) Comparison of the plasmonic loss peaks for the sensors featuring nonuniform and uniform gold layers. In thick solid curves we present losses of a sensor having nonuniform gold film with thickness that varies from 20 to 65 nm. For comparison, in thin dashed curves we present losses of a sensor having uniform 50 nm thick gold film. Data are presented for the two values of biolayer thicknesses $d_{\text{bio}}=0$ and $d_{\text{bio}}=10$ nm.

Another important type of imperfection in the sensor structure could be nonuniformity in the biolayer thickness. Consider as an example a biolayer with thickness that varies from 10 nm close to the bridges to 55 nm in the middle of semicylindrical channels. In this case the thickness of a gold layer is assumed to be uniform and equal to 40 nm. Figure 6 shows plasmonic loss peaks for the case of a nonuniform biolayer, as well as for the cases of two uniform biolayers of thicknesses $d_{\text{bio}}=0$ and $d_{\text{bio}}=10$ nm. In Fig. 6 we see that the nonuniformity of the biolayer thickness does not change the width or the sharpness of a plasmonic peak, while mostly affecting the peak position.

B. Case (b): Tuning of a Microstructured Optical Fiber-Based Sensor Using Defects

We now consider the possibility of tuning transmission losses of the fundamental core mode by using defects in

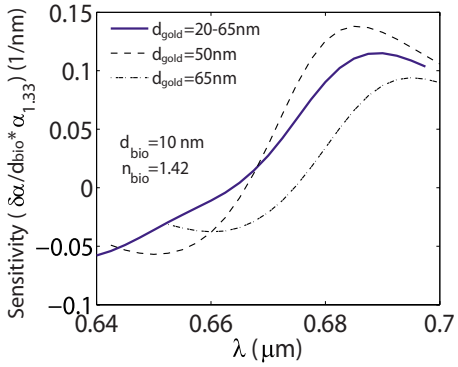

Fig. 5. (Color online) Comparison of sensitivities of the MOF-based sensors having nonuniform gold layer (thick solid curve) and uniform gold layers (thin dashed curves).

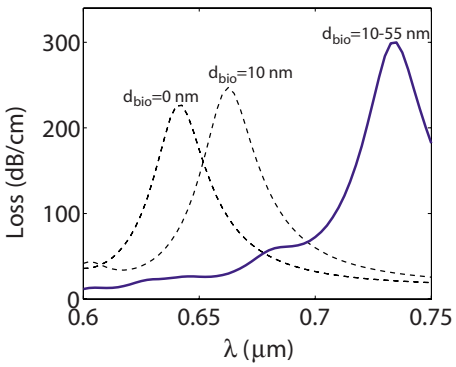

Fig. 6. (Color online) Comparison of the plasmonic loss peaks for the sensors featuring nonuniform and uniform biolayers. In thick solid curves we present losses of a sensor having nonuniform biolayer with thickness that varies from 10 to 55 nm. For comparison, in thin dashed curves we present losses of a sensor having uniform 10 nm thick biolayer, as well as losses of a sensor without biolayer.

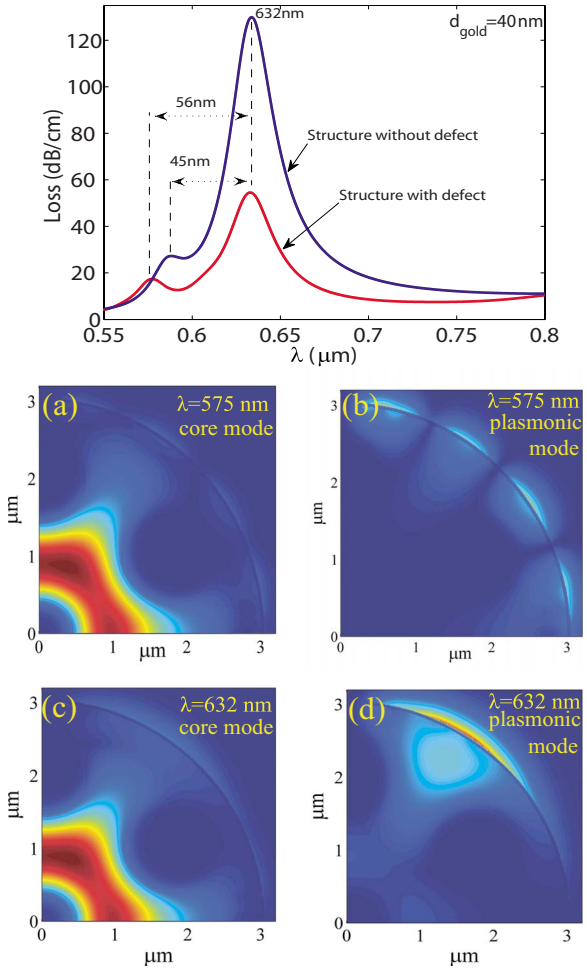

Fig. 7. (Color online) Loss spectra of the fundamental core modes of the two MOFs shown in Fig. 1 (fibers with and without a tuning defect). Both curves are calculated assuming aqueous analyte $n_a=1.33$, gold layer thickness $g_{gold}=40$ nm, and $d_{bio}=0$. Insets (a) and (b) show energy fluxes of the near degenerate core-guided mode and a higher order plasmon mode for the MOF with a defect at the wavelength of a first absorption peak $\lambda=575$ nm. Insets (c) and (d) show energy fluxes of the near degenerate core-guided mode and the fundamental plasmon mode for the MOF with a defect at the wavelength of a second absorption peak $\lambda=632$ nm.

the fiber cross section [see Fig. 1(b)]. Losses of the fundamental core modes for the two MOF structures with and without a defect are presented in Fig. 7. In these simulations we assume $d_{bio}=0$ and $d_{gold}=40$ nm, with the rest of the geometrical parameters described in Subsection 2.A. In Fig. 7 we observe that the absorption spectra of the MOF fundamental modes show two distinct peaks. To understand better the nature of these peaks we consider field distributions of the MOF eigenmodes at the wavelengths corresponding to the peak centers. Particularly, in the vicinity of an absorption peak we always find a near degeneracy between the fundamental core mode and a plasmon mode, which is the main reason for increase in the fundamental core mode absorption losses. In insets (a) and (b) of Fig. 7 we show energy fluxes of the near degenerate core-guided and plasmon modes for the MOF with defects at the wavelength of a first plasmonic peak $\lambda=575$ nm. In insets (c) and (d) we show energy fluxes of the near degenerate core-guided and plasmon modes for the same fiber at the wavelength of a second plasmonic peak $\lambda=632$ nm. At each absorption peak we observe a distinct plasmonic mode having most of its electromagnetic fields delocalized in the analyte region. From the energy flux distributions shown in Fig. 7 we call the plasmonic mode in the vicinity of the second absorption peak "the fundamental plasmonic mode," while we call the plasmonic mode in the vicinity of the first absorption peak "a higher order plasmonic mode."

In Fig. 7 we also observe that the introduction of a structural defect in the MOF cross section in the near vicinity of a gold layer allows one to tune the relative position of the two plasmonic peaks. In planar samples, tuning of the plasmonic peaks is somewhat challenging as the only means for doing so is through variation in the material parameters of a substrate material on which the gold layer is deposited. Thanks to the freedom of making holes in the MOF cross section, tuning of plasmon peaks can be accomplished by locally changing the substrate material properties via introduction of the small air holes.

In Fig. 8 we present amplitude sensitivities of the two MOF-SPR sensors described above. In the vicinity of the first plasmonic peak ($\lambda=600$ nm) the MOF with a defect shows an amplitude sensitivity of 0.0275 nm^{-1}, which is

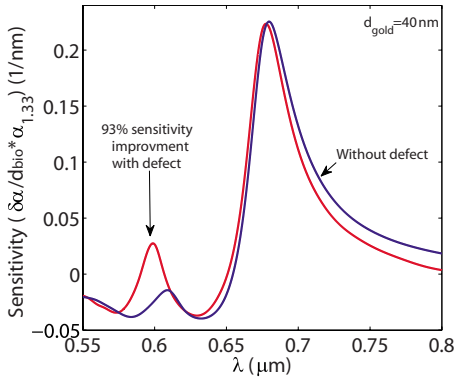

Fig. 8. (Color online) Amplitude sensitivity of the two sensors based on MOFs with and without a defect in their cross section [see Figs. 1(a) and 1(b)]. In both cases $n_a=1.33$, $d_{gold}=40$ nm. Sensor based on the MOF with a defect shows a considerable enhancement of amplitude sensitivity in the vicinity of the first plasmonic peak.

almost twice as high as the amplitude sensitivity of 0.0143 nm^{-1} demonstrated by the MOF without a defect. The resolutions of these two sensors operating in the vicinity of the first plasmonic peak are, respectively, 0.36 and 0.70 nm. In the vicinity of the second plasmonic peak ($\lambda = 680$ nm) sensor sensitivities for the two MOFs with and without a defect are almost identical and equal to ~ 0.22 nm^{-1}, which leads to the sensor resolutions of 0.044 nm.

3. PHOTONIC BANDGAP FIBER-BASED SURFACE PLASMON RESONANCE BIOSENSORS

In Section 2 we have presented sensor designs based on the TIR-guiding MOFs. In this section we present the design of SPR sensors based on photonic bandgap fibers.

In Fig. 9 the schematic of a honeycomb photonic crystal fiber-based SPR sensor is presented. The design parameters are chosen as follows: the center to center distance between the adjacent holes is $\Lambda = 1.33$ μm, the hole diameter is $d = 0.6\Lambda$, and the diameter of the hole in the core center is $d_c = 0.45\Lambda$. The main function of a central hole in the fiber core is to tune the effective refractive index of the core-guided mode. The fiber is made of silica glass with refractive index $n_{glass} = 1.45$, the holes in the fiber cross section are filled with air $n_{air} = 1$, while the large semicircular channels are filled with aqueous analyte $n_a \sim 1.332$ and plated with a 35 nm thick layer of gold. With these parameters, the fiber core supports a leaky core mode confined by the bandgap of a honeycomb reflector. Guided by the bandgap of the fiber reflector, the core mode effective refractive index can be considerably lower than that of a silica material. The radiation loss of the bandgap-guided core mode can be reduced by adding more layers to the honeycomb reflector surrounding the core. The main reason why we chose a honeycomb structure of the fiber reflector is because it enables a large photonic bandgap, thus simplifying phase matching of the core-guided and plasmonic modes.

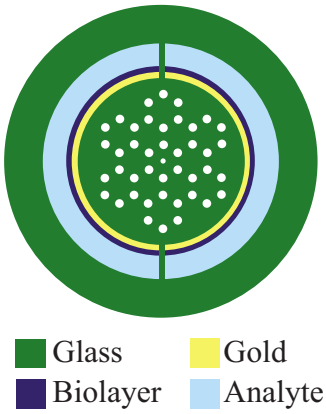

Fig. 9. (Color online) Solid-core photonic bandgap fiber-based SPR sensor. (a) Schematic of a sensor. Solid core having a small central hole is surrounded by the honeycomb photonic crystal reflector. Two large channels are integrated into the fiber cross section to enable analyte access in the vicinity of the fiber core. Analyte channels are gold plated with a $d_{gold} = 35$ nm film. Gold layer is bordered by a biolayer and aqueous analyte.

Figures 10 and 11, respectively, present the dispersion relation and losses of the fundamental core mode and the two plasmonic modes for a structure defined in Fig. 9. Unlike in the case of a planar metal/dielectric interface, which supports a single plasmonic excitation, metallized microstructured fibers can support several plasmonic modes [30]. To demonstrate this point Fig. 10 presents the effective refractive index of the core-guided and plasmon modes as a function of wavelength. Avoided crossing between the core-guided and plasmonic modes is clearly visible in the vicinity of 600 and 920 nm. Not surprisingly, when tracking losses of a core-guided mode as a function

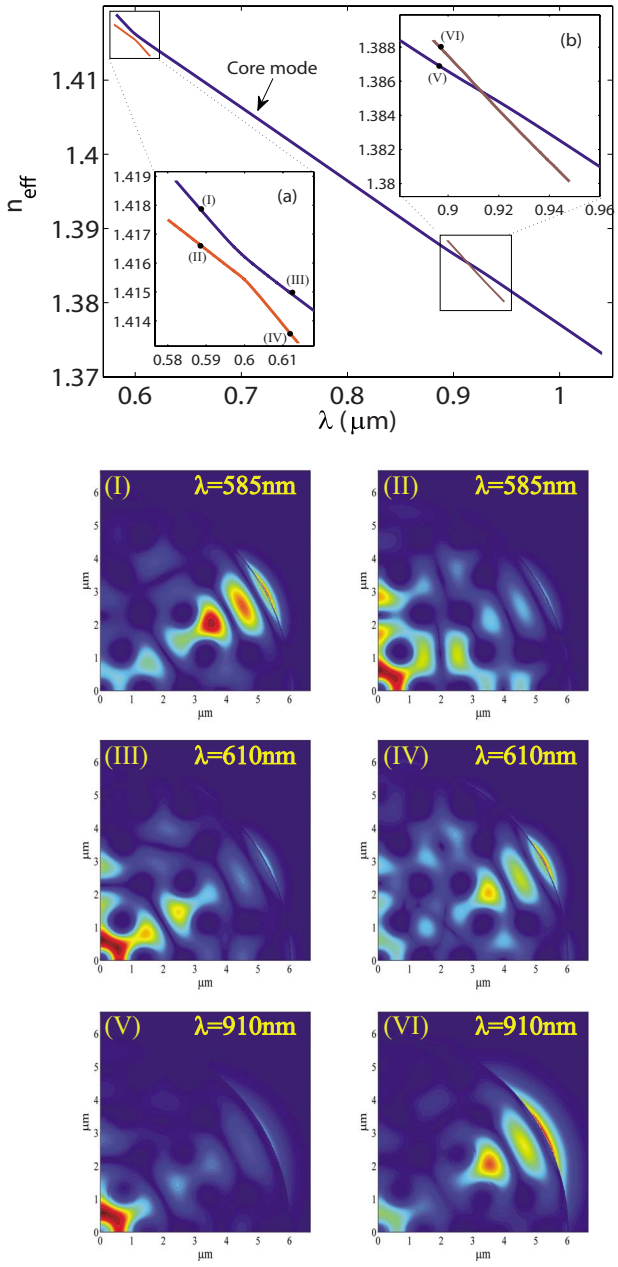

Fig. 10. (Color online) The effective refractive index of the fundamental core mode of a photonic bandgap fiber in the 580–1020 nm spectral region. Insets (I–IV) show strong mixing of the fundamental core mode and a plasmon mode in the vicinity of the first phase matching point $\lambda = 600$ nm. Insets (V) and (VI) show strong mixing of the fundamental core mode and a plasmon mode in the vicinity of the second phase matching point $\lambda = 920$ nm.

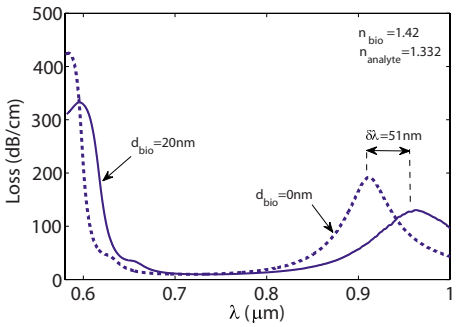

Fig. 11. (Color online) Losses of the fundamental core mode are shown for the cases of zero biolayer thickness (solid curve) and 20 nm thick biolayer (dashed curve).

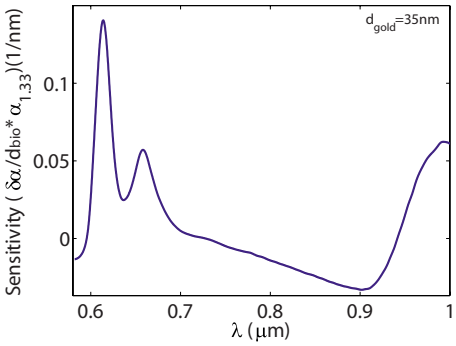

Fig. 12. (Color online) Amplitude sensitivity of the photonic bandgap fiber-based sensor.

of wavelength (see Fig. 11) one observes two absorption peaks at the points of phase matching between the fundamental core and plasmon modes. In principle, simultaneous detection of changes in the position of several plasmonic peaks can improve sensor sensitivity.

In Fig. 11, the solid curve presents loss of the fundamental core mode, assuming zero biolayer thickness $d_{\text{bio}}=0$ nm. The dashed curve in Fig. 11 shows a considerable shift of the fundamental mode absorption spectrum toward longer wavelengths when a 20 nm thick biolayer of refractive index $n_{\text{bio}}=1.42$ is deposited on top of the gold film. Between the two peaks, the second plasmonic peak exhibits the strongest shift ($\delta\lambda=51$ nm) when a biolayer is added. Such a shift defines 2.55 nm nm^{-1} spectral sensitivity of the second peak to changes in the biolayer thickness. Assuming that the 0.1 nm shift in the peak position can be reliably detected, such a sensitivity value defines the sensor resolution of 0.039 nm in the biolayer thickness. Finally, in Fig. 12 we present the sensor amplitude sensitivity. Maximal sensitivity is reached in the vicinity of the first peak and is equal to 0.14 nm^{-1}. Assuming that a 1% change in the peak intensity can be reliably detected, such a sensitivity value defines the sensor resolution of 0.0714 nm in the biolayer thickness.

4. CONCLUSION

In conclusion, we have presented several designs of the SPR sensors of the biolayer thickness based on the microstructured and photonic bandgap fibers. A sensor resolution of the biolayer thickness as low as 0.039 nm is demonstrated in the whole 600–920 nm region. The possibility of having several plasmonic excitations in the spectrum of the same fiber sensor was also demonstrated. Finally, tuning of plasmonic peaks was shown by introducing a defect in the fiber cladding placed in the near vicinity of the metal layer.

ACKNOWLEDGMENTS

This work is supported in part by the Canada Research Chair program, Canada Institute for Photonic Innovations grant FP3, and Natural Sciences and Engineering Research Council (NSERC) (Canada) Strategic grant "Miniaturized Si-based plasmonics platform for gas detection."

REFERENCES

1. V. M. Agranovich and D. L. Mills, *Surface Polaritons-Electromagnetic Waves at Surfaces and Interfaces* (North-Holland, 1982).
2. E. Kretschmann and H. Raether, "Radiative decay of non radiative surface plasmons excited by light," Z. Naturforsch. A **23**, 2135–2140 (1968).
3. B. Liedberg, C. Nylander, and I. Lundstrom, "Surface plasmon resonance for gas detection and biosensing," Sens. Actuators B **4**, 299–304 (1983).
4. J. L. Melendez, R. Carr, D. U. Bartholomew, K. A. Kukanskis, J. Elkind, S. S. Yee, C. E. Furlong, and R. G. Woodbury, "A commercial solution for surface plasmon sensing," Sens. Actuators B **35**, 212–216 (1996).
5. L. M. Zhang and D. Uttamchandani, "Optical chemical sensing employing surface plasmon resonance," Electron. Lett. **24**, 1469–1470 (1988).
6. A. V. Kabashin and P. Nikitin, "Surface plasmon resonance interferometer for bio- and chemical-sensors," Opt. Commun. **150**, 5–8 (1998).
7. A. N. Grigorenko, P. Nikitin, and A. V. Kabashin, "Phase jumps and interferometric surface plasmon resonance imaging," Appl. Phys. Lett. **75**, 3917–3919 (1999).
8. P. Schuck, "Use of surface plasmon resonance to probe the equilibrium and dynamic aspects of interactions between biological macromolecules," Annu. Rev. Biophys. Biomol. Struct. **26**, 541–566 (1997).
9. C. P. Lavers and J. S. Wilkinson, "A waveguide-coupled surface-plasmon sensor for an aqueous environment," Sens. Actuators B **22**, 475–481 (1994).
10. R. Harris and J. S. Wilkinson, "Waveguide surface plasmon resonance sensors," Sens. Actuators B **29**, 261–267 (1995).
11. M. N. Weiss, R. Srivastava, and H. Grogner, "Experimental investigation of a surface plasmon-based integrated optic humidity sensor," Electron. Lett. **32**, 842–843 (1996).
12. J. Homola, J. Ctyroky, M. Skalky, J. Hradiliva, and P. Kolarova, "A surface plasmon resonance based integrated optical sensor," Sens. Actuators B **39**, 286–290 (1997).
13. J. Dostalek, J. Ctyroky, J. Homola, E. Brynda, M. Skalsky, P. Nekvindova, J. Spirkova, J. Skvor, and J. Schrofel, "Surface plasmon resonance biosensor based on integrated optical waveguide," Sens. Actuators B **76**, 8–12 (2001).
14. A. K. Sheridan, R. D. Harris, P. N. Bartlett, and J. S. Wilkinson, "Phase interrogation of an integrated optical SPR sensor," Sens. Actuators B **97**, 114–121 (2004).
15. A. K. Sharma, R. Jha, and B. D. Gupta, "Fiber-optic sensors based on surface plasmon resonance: a comprehensive review," IEEE Sens. J. **7**, 1118–1129 (2007).
16. M. Skorobogatiy and A. Kabashin, "Photon crystal waveguide-based surface plasmon resonance biosensor," Appl. Phys. Lett. **89**, 143518 (2006).
17. M. Skorobogatiy and A. Kabashin, "Plasmon excitation by the Gaussian-like core mode of a photonic crystal waveguide," Opt. Express **14**, 8419–8424 (2006).
18. A. Hassani and M. Skorobogatiy, "Design of the microstructured optical fiber-based surface plasmon

resonance sensors with enhanced microfluidics," Opt. Express **14**, 11616–11621 (2006).
19. A. Hassani and M. Skorobogatiy, "Design criteria for microstructured-optical-fiber-based surface-plasmon-resonance sensors," J. Opt. Soc. Am. B **24**, 1423–1429 (2007).
20. B. Gauvreau, A. Hassani, M. Fassi Fehri, A. Kabashin, and M. A. Skorobogatiy, "Photonic bandgap fiber-based surface plasmon resonance sensors," Opt. Express **15**, 11413–11426 (2007).
21. A. Hassani, B. Gauvreau, M. Fassi Fehri, A. Kabashin, and M. A. Skorobogatiy, "Photonic crystal fiber and waveguide-based surface plasmon resonance sensors for applications in the visible and near-IR," Electromagnetics **28**, 198–213 (2008).
22. A. Hassani, A. Dupuis, and M. Skorobogatiy, "Surface plasmon resonance-like fiber-based sensor at terahertz frequencies," J. Opt. Soc. Am. B **25**, 1771–1775 (2008).
23. X. Zhang, R. Wang, F. M. Cox, B. T. Kuhlmey, and M. C. J. Large, "Selective coating of holes in microstructured optical fiber and its application to in-fiber absorptive polarizers," Opt. Express **15**, 16270–16278 (2007).
24. M. Hautakorpi, M. Mattinen, and H. Ludvigsen, "Surface-plasmon-resonance sensor based on three-hole microstructured optical fiber," Opt. Express **16**, 8427–8432 (2008).
25. P. J. A. Sazio, "Microstructured optical fibers as high-pressure microfluidic reactors," Science **311**, 1583–1586 (2006).
26. X. H. Yang and L. L. Wang, "Silver nanocrystals modified microstructured polymer optical fibers for chemical and optical sensing," Opt. Commun. **280**, 368–373 (2007).
27. H. W. Lee, M. A. Schmidt, H. K. Tyagi, L. Prill Sempere, and P. St. J. Russell, "Optical fiber hybrid-surface plasmon polaritons," Appl. Phys. Lett. **93**, 111102 (2008).
28. M. A. Schmidt, L. N. Prill Sempere, H. K. Tyagi, C. G. Poulton, and P. St. J. Russell, "Waveguiding and plasmon resonances in two-dimensional photonic lattices of gold and silver nanowires," Phys. Rev. B **77**, 033417 (2008).
29. K. Kurihara, K. Nakamura, E. Hirayama, and K. Suzuki, "An absorption-based surface plasmon resonance sensor applied to sodium ion sensing based on an ion-selective optode method," Anal. Chem. **74**, 6323–6329 (2002).
30. S. J. Al-Bader and M. Imtaar, "Optical fiber hybrid-surface plasmon polaritons," J. Opt. Soc. Am. B **10**, 83–88 (1993).